Title
A complete sample of Seyfert galaxies selected at 0.25 keV

Journal
Monthly Notices of the Royal Astronomical Society, 327(2)

ISSN
0035-8711

Authors
Vaughan, S
Edelson, R
Warwick, RS
et al.

Publication Date
2001-10-21

DOI
10.1046/j.1365-8711.2001.04763.x

Peer reviewed

Mon. Not. R. Astron. Soc. **000**, 1–13 (2001) Printed 22 April 2017 (MN LATEX style file v1.4)

A complete sample of Seyfert galaxies selected at 1/4 keV

S. Vaughan[1,2], R. Edelson[1,3], R. S. Warwick[1], M. A. Malkan[3], M. R. Goad[1]

[1] *X-Ray Astronomy Group; Department of Physics and Astronomy; Leicester University; Leicester LE1 7RH; U.K.*
[2] *Institute of Astronomy; Madingley Road; Cambridge CB3 0HA; U.K.*
[3] *Department of Physics and Astronomy; University of California, Los Angeles; Los Angeles, CA 90095-1562; U.S.A.*

Accepted 18/6/2001; submitted 11/4/2001; in original form 7/3/2001

ABSTRACT

We have used the *ROSAT* Bright Source Catalogue to extract a complete sample of sources selected in the band from 0.1–0.4 keV. This 1/4 keV-selected sample is comprised of 54 Seyfert galaxies, 25 BL Lacertae objects, 4 clusters and 27 Galactic stars or binaries. Seyfert-type galaxies with "ultrasoft" X-ray spectra can very often be classed optically as Narrow-line Seyfert 1s (NLS1s). Such objects are readily detected in 1/4 keV surveys; the sample reported here contains 20 NLS1s, corresponding to a 40% fraction of the Seyferts. Optical spectra of the Seyfert galaxies were gathered for correlative analysis, which confirmed the well-known relations between X-ray slope and optical spectral properties (e.g., [O III]/Hβ ratio; Fe II strength, Hβ width). The various intercorrelations are most likely driven, fundamentally, by the shape of the photoionising continuum in Seyfert nuclei. We argue that a steep X-ray spectrum is a better indicator of an "extreme" set of physical properties in Seyfert galaxies than is the narrowness of the optical Hβ line.

The correlation studies were also used to isolate a number of Seyfert galaxies with apparently "anomalous" properties. Of particular interest are the six objects with relatively weak permitted line emission (Hβ and Fe II) and weak optical continua. Such objects are rare in most surveys, but two of these (IC 3599 and NGC 5905) are known to be transient active galactic nuclei in which the X-ray flux has faded by factors $\sim$100. If the other four objects also turn out to be transient, this would demonstrate that 1/4 keV surveys provide an efficient way of finding an interesting class of object.

Finally, the luminosity function of the 1/4 keV-selected Seyfert galaxies was determined and broken down into subsamples to investigate the relative space densities of Seyferts when separated on the basis of either X-ray slope or Hβ line width.

Key words: databases: surveys – galaxies: active – galaxies: Seyfert: general – X-ray: galaxies

1 INTRODUCTION

Although Active Galactic Nuclei (AGN) exhibit an extremely wide variety of properties it has, nevertheless, been posited that such objects can be characterised in terms of a relatively small number of underlying physical parameters. Multi-wavelength observations of well-defined source samples derived from large-area surveys, such as the ultraviolet-excess Palomar Bright Quasar Survey (BQS; Schmidt & Green 1983), have proved a particularly effective means of identifying the key physical drivers in AGN. For instance, a principle component analysis of 87 BQS objects indicated strong correlations between optical Fe II, [O III] λ5007 line strengths and the velocity width and asymmetry of Hβ (Boroson & Green 1992; henceforth BG92). This approach was extended into the X-ray regime by Laor *et al.* (1997) and others, who found correlations between these optical properties and the slope of the soft X-ray continuum (α_X). Most notably, Seyfert galaxies and quasars with very steep soft X-ray spectra – 'ultrasoft' Seyferts, defined here by $\alpha_X > 1.7$ – tend to have narrow Hβ, strong Fe II and weak [O III] lines. Many of these ultrasoft sources are, in fact, Narrow-Line Seyfert 1 (NLS1) galaxies (Boller, Brandt & Fink 1996), a subclass of AGN originally identified on the basis of their strong and narrow permitted line emission (e.g., FWHM H$\beta \leq 2000$ km s^{-1} and [O III]/H$\beta \leq$ 3; Osterbrock & Pogge 1985). The remarkable properties of NLS1 galaxies have often been interpreted as due to an extremal value of some underlying physical parameter, most frequently the mass accretion rate relative to the Eddington limit (BG92; Pounds, Done & Osborne 1995).

Of course, the gross properties of an AGN sample depend critically on the waveband of the original survey. For instance, hard X-ray selection introduces a bias against the detection of objects with a steep X-ray spectrum and therefore against NLS1s. An illustration of this effect is provided by the HEAO-1 A2 hard X-ray survey (Piccinotti *et al.* 1982) which failed to find any ultrasoft or NLS1s. In contrast ultrasoft Seyferts were detected in both the *ROSAT* X-ray (0.1-2.4 keV) and extreme-ultraviolet (EUV; 60–210 eV) all-

sky surveys (e.g., Puchnarewicz *et al.* 1992; Grupe *et al.* 1998a; Pounds *et al.* 1993; Edelson *et al.* 1999; Grupe, Thomas & Beuermann 2001), although the well-studied samples derived from these surveys are either rather small (e.g. Edelson *et al.* 1999), incomplete or biased in favour of sources with a particular spectral form.

In this paper we report on the first large, complete sample of Seyfert galaxies selected in the softest accessible (0.1-0.4 keV) X-ray band (which hereafter is referred to as the 1/4 keV band). The paper is organized as follows. The method used to select the full list of sources from the *ROSAT* survey data is described in § 2 together with the identification of a complete 1/4 keV-selected Seyfert galaxy sample. The statistical properties of the Seyfert galaxy sample are then investigated in § 3. This section includes a detailed study of the correlations which exist between parameters describing the optical to soft X-ray continuum and optical emission line properties of the Seyfert galaxies. A derivation of the luminosity function of the 1/4 keV-selected Seyfert galaxy sample is also presented. § 4 goes on to discuss the implications of our results, followed by a brief summary of the main conclusions of the paper. Two appendices are also included. The first provides source lists and further information relating to the two remaining source subsamples, namely other extragalactic sources (i.e., excluding Seyfert galaxies) and sources with Galactic counterparts. Appendix B gives details of an optical programme carried out at the 4.2m William Herschel Telescope (WHT) on La Palma and the 3.0m Shane Telescope at the Lick Observatory which, together with published data, provides nearly complete optical spectroscopy for the Seyfert galaxy sample. Throughout this work values of $H_0 = 50$ km s^{-1} Mpc^{-1} and $q_0 = 0.5$ are assumed and all measured parameters are quoted for the rest frame of the source.

2 SAMPLE SELECTION

During 1990 *ROSAT* performed an all-sky survey in both the soft X-ray and EUV bands. The former employed the *ROSAT* X-ray telescope and position sensitive detector (PSPC; Trümper *et al.* 1991) and resulted in the *ROSAT* Bright Source Catalogue (RBSC; Voges *et al.* 1999) of 18,811 soft X-ray sources. A high fraction of these X-ray sources are AGN (e.g., Thomas *et al.* 1998; Krautter *et al.* 1999). We utilize the RBSC in deriving a new sample based on a count rate threshold in the 0.1-0.4 keV (i.e. 1/4 keV) *ROSAT* band.

The three selection criteria used to construct a preliminary source list were as follows:

(i) The 0.1–0.4 keV count rate $C \geq 0.25$ ct s^{-1}.

(ii) Galactic column $N_H \leq 1.5 \times 10^{20}$ cm^{-2} (using N_H measurements from Dickey & Lockman 1990).

(iii) Dec $\delta \geq 0^\circ$.

The PSPC C- and H-band (0.1-0.4 keV and 0.5–2.0 keV respectively) count rates, C and H, were derived in an approximate way from the RBSC hardness ratio ($HR1 = (H-C)/(H+C)$) and full-band (0.1–2.4 keV) count rate T:

$$C \approx \frac{(1-HR1)}{2}T$$

$$H \approx \frac{(1+HR1)}{2}T$$

In practice this method recovered the correct values to within 0.01 ct/s compared to the values published in Schwope *et al.* (2000). Criteria (ii) and (iii) delimit the survey area to regions around the Lockman Hole (Lockman, Jahoda & McCammon 1986) totalling ∼0.6 sr (∼ 5% of the sky). Selection in terms of line-of-sight column is crucial; the N_H limit of 1.5×10^{20} cm^{-2} corresponds to a foreground optical depth $\tau \approx 2$ in the 0.1–0.4 keV band. The total number of X-ray sources satisfying the above criteria is 110.

The initial classification of the X-ray sources in our source list was based on the optical identifications of Schwope *et al.* (2000) together with information obtained from the SIMBAD[⋆] and NED[†] on-line catalogues. This analysis showed that the 110 X-ray sources comprise 27 Galactic objects (3 cataclysmic variable stars, 6 white dwarfs, 17 active coronal stars and one super-soft source) and 83 extragalactic objects (54 Seyfert galaxies or quasars, 25 BL Lac objects, 4 clusters of galaxies). Table 1 shows the Seyfert subsample, which is the focus of the present work, but for completeness the full lists of non-Seyfert sources are presented in Appendix A.

In Table 1 the columns provide the following information: (2) The source name; (3) optical type (see § 3.1); (4) the redshift; (5) and (6) the right ascension and declination as tabulated in the RBSC; (7) the full-band count rate; (8) hardness ratio; (9) an X-ray slope (derived as in Edelson *et al.* 1999); (10) Galactic column density; (11) and (12) derived C- and H-band count rates; (13) optical V-band magnitude; (14) reference for the optical information (W indicates WHT data - see Appendix B , S indicates Shane data - see Appendix B, Be indicates data from Bedford, Vilhu & Petrov (1988), G from Grupe *et al.* (1999), L from Lipari, Terlevich & Macchetto (1993), P from Puchnarewicz *et al.* (1995), St from Stephens (1989)). The tabulated information is derived from the published RBSC data (e.g., Voges *et al.* 1999 and Schwope *et al.* 2000) except for the Galactic N_H (Dickey & Lockman 1990).

2.1 Sample completeness

The completeness of the sample was checked using the $\langle V/V_{max}\rangle$ test of Schmidt (1968). For the Seyfert sample $\langle V/V_{max}\rangle = 0.52 \pm 0.04$ indicating no evidence for either strong evolution or incompleteness. The BL Lac sample (Appendix A) shows evidence for either incompleteness or negative evolution, with $\langle V/V_{max}\rangle = 0.37 \pm 0.06$. This effect has been seen in previous samples of X-ray selected BL Lacs, first in the *Einstein* Medium Sensitivity Survey (Maccacaro *et al.* 1984) and also in *ROSAT* selected samples (Bade *et al.* 1998), and may be due to cosmological evolution of some subset of the BL Lac population.

The Galactic sample has $\langle V/V_{max}\rangle = 0.38 \pm 0.06$. This apparent incompleteness is most likely due to the source populations falling below the Euclidean prediction at distances comparable to the scale height of the Galactic disc. In order to check this, distance estimates for 17 of the sources were taken from the literature (e.g., Strassmeier *et al.* 1993; Vennes *et al.* 1997) or derived from the distance moduli of the stars with well-known spectral type. The mean distance to the ten main sequence stars with known distances is ∼ 90 pc, and the mean distance to the older stars (white dwarfs, RS CVn systems) is ∼ 180 pc. These are comparable to the scale heights of the *young thin disc* of the Galaxy (∼ 100 pc) and the *old thin disc* (∼ 300 pc), respectively (e.g., Haywood, Robin &

⋆ http://simbad.u-strasbg.fr/Simbad
† http://nedwww.ipac.caltech.edu/

Table 1. The Seyfert galaxy sample. N_H is in units of 10^{20} cm^{-2}.

No (1)	Name (2)	Type (3)	z (4)	R.A. (J2000) (5)	Dec. (J2000) (6)	T (ct/s) (7)	$HR1$ (8)	α_X (9)	N_H (10)	C (ct/s) (11)	H (ct/s) (12)	m_V (13)	Ref (14)
1	1E 0919+515	NLS1	0.161	09 22 46	51 20 46	0.42±0.03	-0.69±0.05	2.2	1.43	0.354	0.065	17.9	L, St
2	Mrk 110	BLS1	0.035	09 25 12	52 17 16	1.69±0.06	-0.19±0.03	1.2	1.47	1.006	0.685	16.0	BG92
3	US 0656	S1	0.160	09 30 17	47 07 25	0.46±0.03	-0.24±0.07	1.4	1.47	0.283	0.173	16.5	–
4	PG 0953+414	BLS1	0.234	09 56 52	41 15 24	0.95±0.06	-0.55±0.04	1.6	0.79	0.735	0.213	14.5	BG92
5	IRAS 10026	BLS1	0.178	10 05 42	43 32 44	0.66±0.04	-0.61±0.04	1.8	1.08	0.534	0.129	16.5	G
6	RX J1008+46	BLS1	0.388	10 08 30	46 29 57	0.42±0.03	-0.33±0.07	1.2	0.91	0.278	0.140	18.9	W
7	Ton 1187	BLS1	0.07	10 13 03	35 51 31	1.38±0.06	-0.44±0.03	1.7	1.38	0.992	0.386	17.4	G
8	RX J1019+37	NLS1	0.133	10 19 00	37 52 49	0.78±0.04	-0.07±0.05	1.0	1.38	0.415	0.360	15.0	W
9	Mrk 141	BLS1	0.042	10 19 12	63 58 02	0.51±0.04	-0.44±0.06	1.6	1.24	0.364	0.142	15.4	G
10	Mrk 142	NLS1	0.045	10 25 31	51 40 39	1.75±0.06	-0.61±0.02	1.9	1.14	1.406	0.341	16.1	G, L
11	RX J1026+55	BLS1	0.119	10 26 52	55 09 13	0.37±0.03	-0.63±0.05	2.0	0.80	0.304	0.069	17.7	W
12	RE J1034+396	NLS1	0.424	10 34 38	39 38 34	2.66±0.09	-0.74±0.02	2.2	1.02	2.312	0.346	15.6	P
13	RX J1046+52	BLS1	0.499	10 46 14	52 56 00	0.32±0.03	-0.82±0.04	2.6	1.08	0.293	0.029	17.5	W
14	RX J1050+55	BLS1	0.331	10 50 55	55 27 31	0.37±0.03	-0.69±0.05	2.0	0.77	0.316	0.058	17.0	W, G
15	RX J1054+48	BLS1	0.266	10 54 44	48 31 45	0.45±0.03	-0.36±0.06	1.5	1.23	0.309	0.145	15.7	W
16	EXO 1055+60	BLS1	0.150	10 58 30	60 16 02	0.39±0.03	-0.76±0.04	2.0	0.61	0.342	0.047	17.0	G
17	RX J1117+65	BLS1	0.147	11 17 10	65 22 10	0.55±0.03	-0.72±0.03	2.0	1.00	0.469	0.076	16.7	G
18	PG 1116+21	BLS1	0.177	11 19 08	21 19 14	1.03±0.06	-0.48±0.05	1.7	1.28	0.759	0.267	15.2	G
19	EXO 1128+691	NLS1	0.043	11 31 05	68 51 55	1.58±0.05	-0.43±0.02	1.6	1.32	1.129	0.450	16.5	Be
20	RX J1138+57	BLS1	0.116	11 38 49	57 42 45	0.58±0.04	-0.48±0.06	1.6	1.09	0.428	0.150	16.5	W
21	NGC 4051	NLS1	0.002	12 03 08	44 31 54	3.92±0.11	-0.45±0.02	1.7	1.32	2.841	1.077	10.8	L
22	RX J1209+32	NLS1	0.145	12 09 46	32 17 02	0.57±0.06	-0.62±0.09	1.9	1.06	0.458	0.107	17.7	W
23	RX J1226+32	BLS1	0.243	12 26 23	32 44 30	0.37±0.03	-0.38±0.07	1.6	1.41	0.255	0.114	17.2	W
24	RX J1232+49	NLS1	0.262	12 32 20	49 57 31	0.34±0.03	-0.60±0.07	2.0	1.31	0.272	0.068	17.0	W
25	Ton 83	NLS1	0.29	12 33 41	31 01 03	0.50±0.03	-0.52±0.05	1.8	1.35	0.378	0.119	16.2	S
26	MCG +08-23-067	NLS1	0.03	12 36 51	45 39 06	0.53±0.04	-0.27±0.06	1.3	1.37	0.334	0.192	16.0	W
27	IC 3599	NLS1/S2	0.022	12 37 41	26 42 29	5.10±0.11	-0.63±0.01	2.0	1.29	4.152	0.943	15.6	S, G
28	Was 61	BLS1	0.044	12 42 11	33 17 03	0.86±0.04	-0.27±0.04	1.1	1.33	0.545	0.313	15.4	S, G
29	RX J1244+58	NLS1	0.198	12 44 41	58 56 29	0.33±0.04	-0.78±0.05	2.1	1.21	0.293	0.036	18.0	W
30	RX J1258+23	BLS1	0.075	12 58 51	23 55 32	0.43±0.03	-0.38±0.06	1.5	1.30	0.297	0.133	17.0	W
31	RX J1312+26	BLS1	0.06	13 12 59	26 28 25	0.42±0.04	-0.41±0.07	1.4	1.05	0.295	0.123	16.8	S, G
32	Ton 1571	NLS1	0.075	13 14 22	34 29 40	0.65±0.04	-0.63±0.04	1.9	0.99	0.530	0.120	16.3	S
33	RX J1319+52	NLS1	0.092	13 19 57	52 35 33	0.66±0.04	-0.52±0.05	1.7	1.19	0.504	0.159	17.3	W
34	RX J1328+24	BLS1	0.223	13 28 20	24 09 27	0.32±0.03	-0.66±0.07	2.0	1.16	0.261	0.053	17.7	W
35	IRAS 13349+243	BLS1	0.108	13 37 18	24 23 06	2.53±0.09	-0.65±0.02	2.0	1.16	2.085	0.442	15.0	S
36	RX J1339+40	NLS1	0.118	13 39 28	40 32 29	0.35±0.03	-0.58±0.06	1.7	0.87	0.276	0.073	17.7	W
37	RX J1342+38	BLS1	0.176	13 42 31	38 29 08	0.37±0.03	-0.37±0.06	1.5	0.91	0.250	0.115	18.0	W
38	PG 1341+25	BLS1	0.087	13 43 56	25 38 45	0.50±0.04	-0.56±0.06	1.8	1.09	0.393	0.111	16.6	W
39	Mrk 663	S2	0.026	13 54 20	32 55 47	0.84±0.05	0.36±0.05	0.4	1.24	0.267	0.568	14.6	S
40	RX J1355+56	BLS1	0.122	13 55 15	56 12 44	0.55±0.06	-0.55±0.08	1.8	1.13	0.423	0.123	17.1	S, G
41	PG 1402+261	BLS1	0.164	14 05 16	25 55 36	0.65±0.04	-0.54±0.05	1.9	1.47	0.500	0.149	15.6	S, L
42	PG 1415+451	BLS1	0.114	14 17 00	44 55 56	0.50±0.03	-0.66±0.03	2.0	1.22	0.413	0.085	15.7	S, L
43	RX J1426+39	S1	0.081	14 26 30	39 03 48	0.36±0.03	-0.54±0.05	1.6	0.93	0.279	0.083	16.0	–
44	Mrk 684	NLS1	0.046	14 31 04	28 17 16	0.58±0.04	-0.23±0.06	1.4	1.48	0.355	0.222	15.2	S
45	Mrk 478	NLS1	0.079	14 42 07	35 26 32	5.78±0.10	-0.70±0.01	2.1	1.03	4.916	0.867	15.0	G, L
46	PG 1444+407	BLS1	0.267	14 46 45	40 35 10	0.34±0.03	-0.57±0.05	1.8	1.25	0.269	0.074	16.0	S
47	RX J1448+35	BLS1	0.113	14 48 25	35 59 55	0.37±0.03	-0.71±0.06	2.1	1.07	0.312	0.053	16.4	W
48	NGC 5905	H II	0.011	15 15 23	55 30 57	0.31±0.02	-0.99±0.01	3.6	1.44	0.308	0.002	12.5	S
49	RX J1529+56	BLS1	0.099	15 29 07	56 16 04	0.74±0.03	-0.43±0.03	1.7	1.29	0.531	0.212	15.8	W
50	MCG +06-36-003	BLS1	0.070	16 13 01	37 16 56	0.42±0.03	-0.31±0.06	1.4	1.24	0.272	0.143	15.5	W
51	RX J1618+36	NLS1	0.034	16 18 09	36 19 50	0.85±0.03	-0.43±0.03	1.6	1.28	0.608	0.242	16.9	S, G
52	RX J1619+40	BLS1	0.038	16 19 51	40 58 34	0.51±0.03	-0.54±0.04	1.6	0.93	0.393	0.117	16.0	S, W
53	RX J1629+40	BLS1	0.272	16 29 01	40 07 53	0.79±0.03	-0.79±0.02	2.3	0.85	0.702	0.082	19.0	S
54	RX J1646+39	NLS1	0.10	16 46 25	39 29 21	0.40±0.03	-0.42±0.06	1.6	1.31	0.281	0.115	17.1	S, G

Creze 1997; Vallenari, Bertelli & Schmidtobreick 2000 and references therein).

3 ANALYSIS

In order to measure the optical properties of the *complete* sample of Seyfert galaxies, new optical spectra have been acquired for 38 of the 54 objects listed in Table 1 (labelled as W or S in column 14 of the Table). These data, when combined with the previously published optical work and non-simultaneous *ROSAT* survey data, provide detailed information about the properties of the Seyfert sample. Details of the new optical observations and the optical data reduction are given in Appendix B.

The full optical dataset was used to define the global properties of the sample, as described in the next subsection, and to search for correlations between the various observed properties as discussed in Section 3.2. Section 3.3 considers the objects which lie at extreme ends of these correlations. Finally the luminosity functions of the complete sample of Seyfert galaxies and of various subsamples of objects are derived in section 3.4.

3.1 General sample properties

The Seyfert galaxy sample comprises roughly equal numbers of "ultrasoft" $\alpha_X > 1.7$, sources (28) and "normal" spectrum objects (26) with an overall mean $\langle \alpha_X \rangle = 1.73$. The sample can also be divided on the basis of Hβ line width. Twenty objects conform to the standard definition of an NLS1 leaving 31 broad-line Seyfert 1s (BLS1s) or Seyfert 2s (including one H II galaxy) and two objects for which Hβ measurements are not available. (Two objects appear to be transient in nature, and hence their exact identification is non-trivial, but have been left in the Seyfert sample. These are discussed further in § 3.3.) The mean redshift of the Seyfert sample is $\langle z \rangle = 0.134$ with a standard deviation of 0.103.

3.2 Correlations between parameters

Correlation tests were first applied to pairs of parameters. In each trial two non-parametric correlation parameters were calculated, namely the Spearman rank-order correlation coefficient R_S and the Kendall τ statistic (see Press *et al.* 1992); the results of the Spearman rank-order tests are shown in Table 2. Each entry contains the R_S (top) and the number of objects (bottom) included in the trial. Those with Spearman rank probabilities $P_S < 0.01$ are marked in **bold**. At this level of significance, $\lesssim 1$ spurious correlations might be expected by chance from 55 trials. Figures 1 and 2 show correlation diagrams for various parameters.

In total, from 55 trials, 8 correlations were found with two-sided probabilities $P_S < 0.01$. However, of these significant correlations, two merely represent trivial correlations between two different measures of the same property (relative strength of [O III] to Hβ, and Fe II strength). All six non-trivial correlations are shown in Figure 1.

Caution must be applied when interpreting the remaining correlations as there is an inherent luminosity bias in the data. In the lowest luminosity objects there is often significant contribution from the host galaxy emission. The extreme cases of MCG+08-23-067, IC 3599, RX J1258+23, Mrk 663 and NGC 5905 show Ca II H and K absorption features from the host galaxy emission (see Vaughan 2001). As a result these objects tend to show redder optical spectra (higher α_{opt} values; see Figure 1e). The other potential difficulty with the current dataset is that the optical and X-ray observation were separated by a time interval of roughly nine years. As ultrasoft Seyferts are often highly variable this may introduce a large uncertainty in the derived values of α_{OX} for individual sources, although the mean for the sample should be robust. Also, the non-simultaneity of the X-ray and optical data may reduce the significance of some of the underlying X-ray/optical correlations.

The well-known anti-correlation between FWHM Hβ and α_X is only weak in the present data ($R_S = -0.31$; $P = 0.03$). One reason for the weakness of the correlation may be the non-simultaneity of the data, as noted above. But it is also important to recognize that the relation between Hβ width and α_X is not necessarily one-to-one, but probably results instead from a 'zone of avoidance,' i.e., virtually all ultrasoft Seyferts have relatively narrow Hβ, whereas optically defined NLS1s can have a wide variety of X-ray slopes. This can be seen Figure 1h (see also Boller, Brandt & Fink 1996) where there is only one ultrasoft Seyfert (RX J1026+55) with broad Hβ. The absence of ultrasoft Seyferts with broad Hβ is not the result of selection effects since the present sample is complete in terms of soft X-ray flux and includes no obvious optical selection bias.

It should also be noted that the correlation is stronger in the higher luminosity sources, as was also the case in the Grupe *et al.* (1999) sample. For the 25 objects with $\nu L_{1/4} < 10^{44.3}$ erg s^{-1} the correlation is weak ($R_S = -0.26$; $P_S = 0.20$) whereas it for the 26 objects with $\nu L_{1/4} > 10^{44.3}$ erg s^{-1} it is strong ($R_S = -0.58$; $P_S = 0.002$).

There is no sigificant correlation between the width of Hβ and the strength of Fe II. Such a correlation has been claimed by Wills (1982), Zheng & O'Brien (1990) and Boroson & Green (1992), however, as discussed in Gaskell (1985) and Gaskell (2000), this is a result of how the strength of Fe II is measured. The quantity Fe II/Hβ has been seen to correlate with FWHM Hβ, but this is due to EW Hβ decreasing as the line gets narrower. No correlation is seen if FWHM Hβ is compared directly with EW Fe II. The lack of correlation between Hβ width and Fe II strength (when measured independently of Hβ) has been confirmed by Grupe *et al.* (1999), Véron-Cetty, Véron & Gonçalves (2001) (see their section 3.3.1) and the present work.

3.2.1 Principal Component Analysis

A Principal Component Analysis (PCA) was applied to the data in an attempt to separate independent sets of correlations. In essence, PCA defines a new coordinate system, defined by a set of eigenvectors called the principal components, which best describe the variance in the data. The first principal component (PC1) explains the largest fraction of variance in the data, the second (PC2) explains the largest fraction of the remaining variance, and so on. The motivation behind PCA is to extract groups of meaningful, independent correlations from a complex dataset. Francis & Wills (1999) and Francis *et al.* (1992) provide brief descriptions of PCA as applied to quasar spectra.

Table 3 reports the first three principal components of an analysis of 8 parameters (as is standard in such analyses, the ranked data were used to reduce the effect of outlying objects and allow for non-linear correlations). Only the 37 objects with measurements of all 8 parameters were used in the analysis (this necessarily excludes some of the most extreme objects with only upper limits on [O III] emission).

The analysis was applied to various sets of input data, with the number of input parameters varied from 7 to 12. In each

Table 2. Results of non-parametric correlation tests. Each entry shows the Spearman rank-order correlation coefficient R_S and the number of objects included in the test. Correlations significant at the $> 99\%$ level are shown in bold.

(1)	Hβ FWHM (2)	[O III] FWHM (3)	EW Fe II (4)	Hα/ Hβ (5)	peak [O III]/Hβ (6)	Fe II/ Hβ (7)	[O III]/ Hβ (8)	α_{opt} (9)	α_{OX} (10)	α_X (11)
$\log(\nu L_{1/4})$	0.26 (51)	0.33 (42)	0.13 (48)	0.16 (39)	-0.23 (35)	-0.14 (47)	**-0.43** (43)	**-0.63** (42)	-0.18 (54)	0.24 (54)
Hβ FWHM		-0.14 (40)	-0.13 (47)	0.10 (39)	0.40 (35)	-0.16 (47)	-0.06 (43)	-0.03 (41)	0.21 (51)	-0.31 (51)
[O III] FWHM			0.13 (40)	0.03 (36)	-0.40 (32)	0.04 (39)	-0.19 (40)	-0.36 (38)	0.02 (41)	0.07 (42)
EW Fe II				-0.32 (38)	-0.37 (35)	**0.84** (47)	**-0.48** (42)	**-0.50** (42)	0.27 (48)	**0.45** (48)
Hα/ Hβ					0.10 (31)	-0.16 (39)	0.36 (36)	0.25 (37)	-0.07 (39)	0.08 (39)
peak [O III]/Hβ						-0.14 (35)	**0.72** (35)	0.29 (31)	-0.35 (35)	**-0.53** (35)
Fe II/ Hβ							-0.30 (42)	-0.30 (41)	0.16 (47)	-0.28 (47)
[O III]/ Hβ								-0.20 (42)	-0.33 (43)	-0.20 (43)
α_{opt}									-0.02 (42)	-0.33 (42)
α_{OX}										-0.08 (54)

case the first two principal components explained greater than 50% of the total variance. PC1 was most closely associated with α_{opt}, [O III]/Hβ and $\nu L_{1/4}$ and least associated with FWHM Hβ, whereas PC2 appears dominated by the FWHM Hβ–α_X relation. PC3 appears to represent the variance in α_{OX} and is the only remaining component to have an eigenvalue above 1 (sometimes considered to be an indicator of the significance of a component). The ordering of PC2 and PC3 was reversed in some of the tests, and they can be seen to contribute almost equally to the total variance. These results closely match those of Grupe *et al.* (1999). Indeed, when the PCA was repeated using exactly the same input parameters as those used by Grupe *et al.* (1999) the same PC1 was found. However, the non-simultaneity of the optical/X-ray data, and the luminosity bias noted above, hamper the interpretation of these principal components.

Table 3. Results of PCA. The relative significances of the first three principal components are listed, as well as their projections onto the original input parameters.

	PC1	PC2	PC3
Eigenvalue	2.72	1.53	1.46
Percentage variance	34.01	19.19	18.36
Cumulative	34.01	53.21	71.56
α_X	0.52	0.59	-0.20
$\nu L_{1/4}$	0.71	-0.17	0.53
FWHM Hβ	0.00	-0.87	-0.18
EW Hβ	0.66	-0.48	-0.18
EW Fe II	0.62	0.24	-0.43
[O III]/Hβ	-0.72	-0.05	0.38
α_{opt}	-0.78	0.05	-0.25
α_{OX}	0.06	-0.32	-0.83

3.3 Outlying Seyferts

Figure 2 shows a correlation diagram with individual outlying objects marked. Four objects in particular stand out as Fe II-strong, [O III]-weak objects with blue optical spectra, these objects are: PG 1402+261, PG 1415+451, Mrk 684 and PG 1444+407. These lie at the extreme negative end of the PC1 defined by BG92 (see BG92 and Kuraszkiewicz *et al.* 2000a). However, of these objects only Mrk 684 conforms to the standard definition of an NLS1, with FWHM Hβ<2000 km s^{-1}, although the other three have ultrasoft X-ray spectra.

At the other end of the parameter space there is a group of six objects which stand out, these are: MCG+08-23-067, IC 3599, Was 61, RX J1258+23, Mrk 663 and NGC 5905. These all tend to possess stronger forbidden than permitted line emission ([O III]/Hβ>1) and weak (and therefore redder, due to host galaxy emission) optical continua when compared to soft X-rays ($\alpha_{OX} > 1.5$). However, with the exception of Mrk 663, which shows no detectable Hβ emission, none of these objects have [O III]/Hβ>3, a commonly used criterion for classifying Seyfert 2s. Only two of these objects stand out from the α_X distribution; NGC 5905 had a remarkably steep soft X-ray spectrum at the time of the *ROSAT* survey, while Mrk 663 shows the hardest spectrum in the 1/4 keV sample. Mrk 663 is probably therefore the only candidate Seyfert 2 in the present sample besides the transient IC 3599.

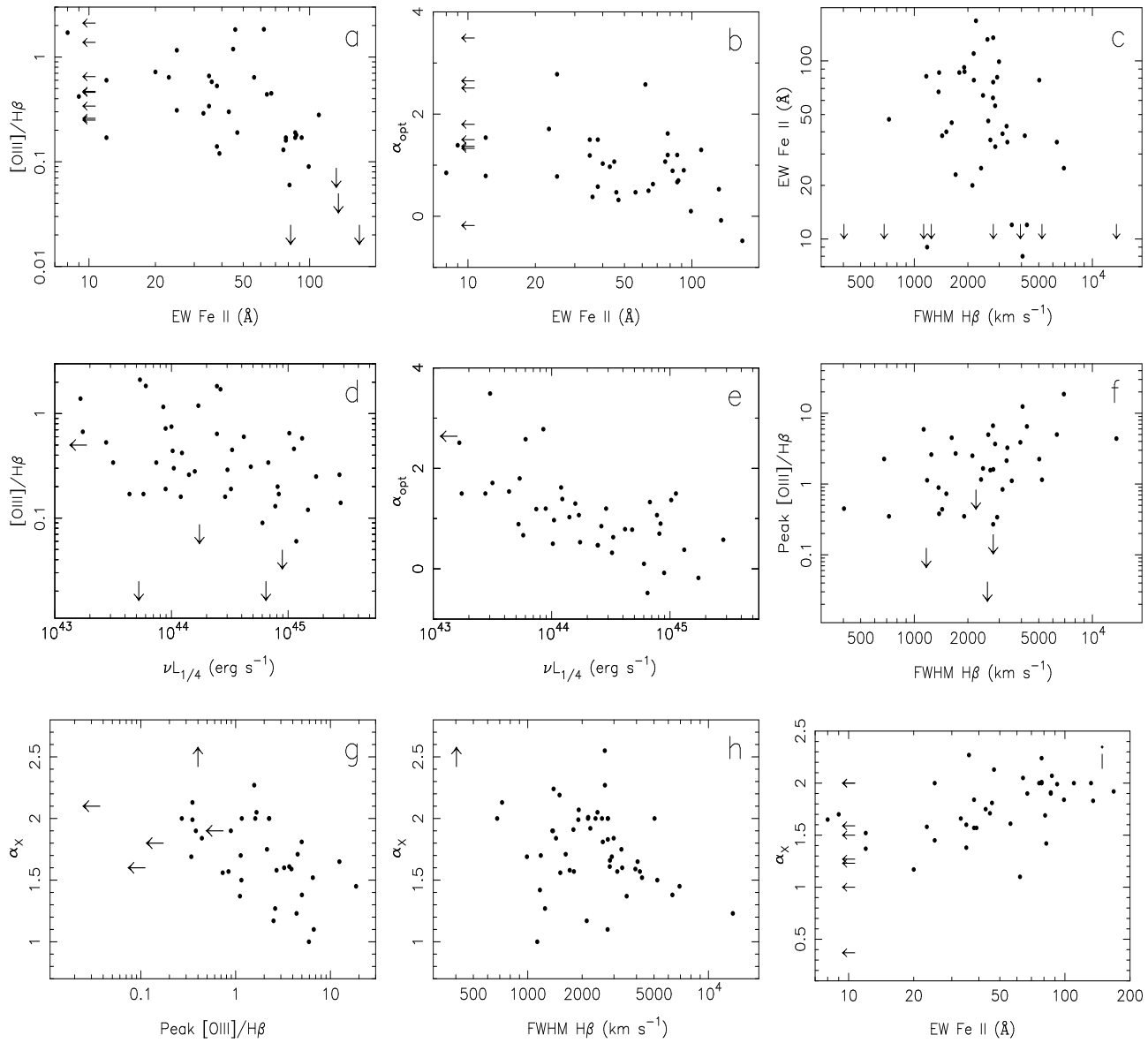

Figure 1. Correlation diagrams for various optical and X-ray parameters. Arrows indicate no detection in the case of Fe II and 1σ limits for undetected [O III]. NGC 5905 has the steepest α_X and is represented by an up arrow in panels g and h, it is also the lowest luminosity object as is indicated by the left arrow in panels d and e.

Both IC 3599 and NGC 5905 have been identified as X-ray transient AGN (e.g., Grupe *et al.* 1995; Brandt, Pounds & Fink 1995; Bade, Komossa & Dahlem 1996; Komossa & Bade 1999). Both objects seem to have been detected by *ROSAT* during some kind of nuclear outburst and have in recent years 'switched off,' showing a substantial drop in their X-ray and optical continua as well as broad and high-excitation line emission. IC 3599 was originally identified as a NLS1 (see Brandt, Pounds & Fink 1995) but now shows only very weak and narrow permitted lines, while NGC 5905 now resembles an H II region more than a Seyfert galaxy. The striking similarity of the optical spectrum of the other weak-Hβ objects to the two known transient AGN raises the interesting question of whether these objects also exhibit X-ray transient behaviour (as noted earlier the optical spectroscopy presented here was taken 9 years after the *ROSAT* survey). In this scenario the X-ray continuum has decreased since the *ROSAT* survey, along with the optical continuum and permitted line emission[‡].

3.4 The Seyfert Galaxy Luminosity Function

The information given in Tables 1 and B1 has been used to derive the luminosity function of the 1/4 keV-selected Seyfert galaxy sample. The luminosity function was calculated using the $1/V_{max}$ method of Schmidt (1968):

‡ Mrk 663 was detected by the *ROSAT* HRI during a 3.1 ksec pointed observation in 1995 at a count rate of ~ 0.2 ct s^{-1}. This is comparable with the PSPC count rate observed during the *ROSAT* survey and suggests that Mrk 663 is a persistent X-ray source.

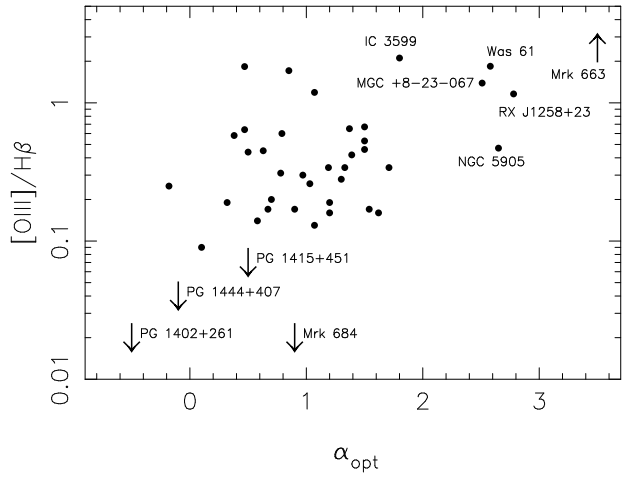

Figure 2. Correlation diagram revealing objects which lie at the extremes of the parameter space.

$$\Phi(L) = \frac{1}{\Delta L} \sum_{i=1}^{N} \frac{1}{V_{max\,i}},$$

Here the luminosity $\nu L_{1/4}$ is taken to be the monochromatic luminosity at 1/4 keV in the rest-frame of the source, in νL_ν units (assuming spectral model comprising a $\alpha_X = 2$ power-law modified by Galactic absorption) .The $\nu L_{1/4}$ values are tabulated for each source in Table B1. For a survey at 1/4 keV, the V_{max} calculation is greatly complicated by the variation of the Galactic foreground absorption across the sky. A similar problem was encountered by Edelson *et al.* (1999) when considering the luminosity function of the AGN discovered in the *ROSAT* WFC survey and here we employed the same approach in evaluating the effective survey volume.

For each source, V_{max} was estimated as:

$$V_{max_i} = \int_0^{N_{Hlim}} \frac{1}{3}\Omega(N_H)\left(\frac{T(N_H)}{T(N_{H_i})}\right)^{\frac{3}{2}} d_i^3 \left(\frac{C_i}{C_{lim}}\right)^{\frac{3}{2}} dN_H,$$

The function $\Omega(N_H)$ represents the differential sky area as a function of Galactic N_H. The integral $\int \Omega(N_H) dH_H$ represents the area of sky actually surveyed whereas the integral $\int \Omega(N_H) T(N_H)^{\frac{3}{2}} dN_H$ gives the equivalent area of *unabsorbed* sky. For the present survey the latter integral is 4.8×10^{-2} steradians or 157 square degrees (whereas integration of $\Omega(N_H)$ between the same limits gives $\sim$0.6 steradians). The integrations were carried out over the northern hemisphere only, as the sample is restricted to $\delta \geq 0^\circ$.

Figure 3 shows the resulting luminosity function binned into logarithmic luminosity intervals and and Table 4 lists the corresponding numerical information. (Note this analysis range excludes the sources NGC 4051 and NGC 5905 which have unusually low luminosities, $\nu L_{1/4} < 10^{42}$ erg s^{-1}.) The error bars were calculated using the prescription of Marshall (1985). The luminosity function we derive for full sample of 1/4 keV-selected Seyferts is entirely consistent with that previously calculated for the WFC-selected AGN (Edelson *et al.* 1999).

Next the sample was divided into subsamples and luminosity functions of each subsample calculated. The ratio of the two luminosity functions then gives the relative of space densities as a function of luminosity. The middle panel of Figure 3 shows this when the Seyferts were split into subsamples on the basis of Hβ width (i.e. NLS1 versus BLS1) or X-ray spectral slope ("ultrasoft" versus "normal" spectrum objects) as discussed in Section 3.1.

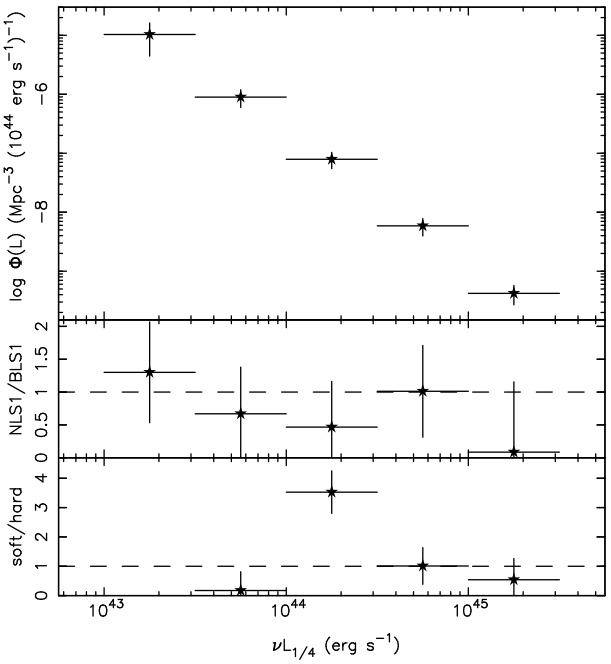

Figure 3. Luminosity function of the 1/4 keV-selected Seyfert galaxies. The top panel shows the function for the complete sample. The middle panel shows the ratio of luminosity functions when the sample is divided into narrow- and broad-line Seyfert 1s. The lower panel shows the ratio when the sample is divided on the basis of X-ray spectral slope. The binning is every half-decade in luminosity.

The ratio of the space densities of NLS1s and BLS1s is formally consistent with a constant over the range of luminosities probed. It is somewhat more difficult to interpret the incidence of ultrasoft Seyferts. In the present sample there are no such objects in the luminosity range $\log(\nu L_{1/4}) = 43.0 - 43.5$ and the next highest luminosity bin there is the suggestion of incompleteness (see Table 4). If we focus on the $\log(\nu L_{1/4}) = 44.0 - 45.5$ range the relative number of ultrasoft objects appears to decrease with luminosity. Interestingly a deficit of ultrasoft Seyferts at high luminosities might be expected due to the effects of the 'K-correction.' Basically the steep spectrum objects will be harder to detect at higher redshifts due the decrease in flux *observer's frame* flux by a factor $(1+z)^{\alpha-1}$, where α is the spectral index; in effect the bright soft X-ray emission is being redshifted out of the observing band. Unfortunately the statistical limitations of the present sample mitigate against a more detailed quantitative analysis of this point.

To date only two NLS1s have been reported at a redshift $z > 0.5$ namely the quasar E 1346+266 with $z = 0.92$, which shows optical and X-ray spectra characteristic of NLS1s (Puchnarewicz, Mason & Cordova 1994), and RX J2241-44 at $z = 0.55$ (Grupe *et al.* 1998a). Of the 69 spectroscopically identified AGN in the deep *ROSAT* surveys of the Lockman Hole (Hasinger *et al.* 1998; Schmidt *et al.* 1998) only one can be postively identified with an NLS1 (at $z = 0.462$; Hasinger *et al.* 2000).

Table 4. Luminosity functions for the 1/4 keV sample. $\Phi(L)$ is in units of Mpc$^{-3}(10^{44}$ erg s$^{-1})^{-1}$.

$\log(\nu L_{1/4})$	All Seyferts						
(erg s^{-1})	$\Phi(L)$	$\langle V/V_{max}\rangle$	N				
(1)	(2)	(3)	(4)	(5)	(6)	(7)	(8)
43.0-43.5	$2.2 \pm 1.3 \times 10^{-6}$	0.58 ± 0.13	5				
43.5-44.0	$6.1 \pm 2.0 \times 10^{-7}$	0.41 ± 0.08	12				
44.0-44.5	$1.7 \pm 0.5 \times 10^{-7}$	0.53 ± 0.08	13				
44.5-45.0	$4.0 \pm 1.5 \times 10^{-8}$	0.58 ± 0.08	13				
45.0-45.5	$9.1 \pm 3.3 \times 10^{-9}$	0.58 ± 0.10	9				
	NLS1s			BLS1s			NLS1/
	$\Phi(L)$	$\langle V/V_{max}\rangle$	N	$\Phi(L)$	$\langle V/V_{max}\rangle$	N	BLS1
43.0-43.5	$6.4 \pm 5.1 \times 10^{-7}$	0.46 ± 0.20	2	$4.9 \pm 3.6 \times 10^{-7}$	0.54 ± 0.20	2	1.3 ± 0.8
43.5-44.0	$2.2 \pm 1.2 \times 10^{-7}$	0.19 ± 0.11	6	$3.3 \pm 1.7 \times 10^{-7}$	0.57 ± 0.13	5	0.7 ± 0.7
44.0-44.5	$5.4 \pm 3.2 \times 10^{-8}$	0.68 ± 0.17	3	$1.2 \pm 0.4 \times 10^{-7}$	0.48 ± 0.09	10	0.5 ± 0.7
44.5-45.0	$1.8 \pm 0.8 \times 10^{-8}$	0.52 ± 0.12	6	$2.0 \pm 0.9 \times 10^{-8}$	0.59 ± 0.12	6	1.0 ± 0.7
45.0-45.5	$7.1 \pm 7.1 \times 10^{-10}$	0.53 ± 0.29	1	$8.4 \pm 3.2 \times 10^{-9}$	0.58 ± 0.10	8	0.1 ± 1.1
	ultrasoft			hard			soft/
	$\Phi(L)$	$\langle V/V_{max}\rangle$	N	$\Phi(L)$	$\langle V/V_{max}\rangle$	N	hard
43.0-43.5	—	—	0	$2.2 \pm 1.3 \times 10^{-6}$	0.58 ± 0.13	5	—
43.5-44.0	$9.0 \pm 4.7 \times 10^{-8}$	0.11 ± 0.14	4	$5.2 \pm 2.0 \times 10^{-7}$	0.55 ± 0.10	8	0.2 ± 0.6
44.0-44.5	$1.3 \pm 4.7 \times 10^{-7}$	0.57 ± 0.10	9	$3.7 \pm 2.3 \times 10^{-8}$	0.54 ± 0.17	3	3.5 ± 0.7
44.5-45.0	$2.3 \pm 8.1 \times 10^{-8}$	0.52 ± 0.09	10	$2.3 \pm 1.2 \times 10^{-8}$	0.61 ± 0.14	4	1.0 ± 0.6
45.0-45.5	$3.2 \pm 1.8 \times 10^{-9}$	0.56 ± 0.14	4	$5.9 \pm 2.8 \times 10^{-9}$	0.59 ± 0.13	5	0.5 ± 0.7

4 DISCUSSION

This paper presents a new sample of soft X-ray bright Seyfert galaxies. The sample is the first to be selected in the $\sim 1/4$ keV *ROSAT* band and is statistically complete.

The analysis reported in Section 3.2 reveals correlations between the soft X-ray spectral slope α_X and the optical [O III] and Fe II line strengths, and the previously known relation between α_X and FWHM Hβ. These relationships appear more like zones of avoidance than linear correlations (see also Section 4.2 of Lawrence *et al.* 1997). A steep X-ray slope (e.g., $\alpha_X \gtrsim 1.7$) seems to be a prerequisite for strong Fe II (EW>100Å) and is almost invariably accompanied by strong, narrow Hβ (FWHM H$\beta \lesssim$3000 km s^{-1}; Peak [O III]/H$\beta \lesssim$0.5). Given the non-simultaneity of the optical/X-ray data and the significant soft X-ray variability exhibited by the source population, these relationships must be intrinsically strong to remain apparent in the current analysis.

The link between α_X and the optical parameters therefore seems to be driving the correlations responsible for the first principal component of BG92 (which is dominated by the strength of [O III] and Fe II and to a lesser extent FWHM Hβ). This is supported by the strong correlation between BG92 PC1 and X-ray slope found by Brandt & Boller (1998). Thus it appears that the high energy continuum, and the slope of the soft X-ray spectrum in particular, are driving many of the relationships observed in optical correlation analyses. This is perfectly reasonable since the physical conditions of the line-emitting plasma will be strongly effected by the incident high-energy continuum. A similar conclusion was reached by Kuraszkiewicz *et al.* (2000b), who explained the different ultraviolet emission properties of a small sample of NLS1s as an effect of the different photoionising continuum in these objects.

The ultrasoft Seyferts, defined by their steep X-ray spectra, are also characterised by extreme values of other observables. The high energy continuum is more closely linked to the underlying accretion processes than are the optical line ratios/widths. However, it is the overlapping class of optically defined NLS1s that have received particular attention, largely on the basis of exceptional X-ray properties in many ultrasoft examples (e.g., Boller *et al.* 1993; Pounds, Done & Osborne 1995). It is now clear that Seyferts selected on the basis of Hβ line width span a range of observed properties, many showing spectra otherwise characteristic of 'normal' Seyfert 1s; the present analysis confirms that optically defined NLS1s do not show enhanced Fe II emission compared to BLS1s, as has been previously suggested. The shape of the high energy continuum is therefore a much more direct indicator of the primary driving processes in AGN than is the width of Hβ. The present sample then represents the ideal one in which to search for extremes of behaviour.

Seyferts with weak permitted line emission (e.g., Hβ and Fe II) sit at at one end of the observed correlations. These are generally rare in soft X-ray surveys, yet the present sample contains a number of such objects. Two of these are known to be X-ray transient and it is plausible that other Hβ-weak Seyferts in the sample are transient in nature. This hypothesis clearly needs to be tested with repeat X-ray and optical observations. If a significant number of the 1/4 keV-selected sources are confirmed as X-ray transients then this would suggest that, at least for a significant fraction of the population, the ultrasoft Seyfert state may be a relatively short-lived one.

The alternative explanation, namely that these objects have not changed significantly since the *ROSAT* survey, is equally interesting. Puchnarewicz & Mason (1998) and Grupe *et al.* (1998b) discuss soft X-ray selected Seyferts which appear to show optical reddening but no X-ray absorption. One possible solution is that these objects all contain dusty, ionised gas along the line-of-sight. The small dust grains are needed to redden the optical continuum, while the surrounding gas is ionised and so produces no soft X-ray absorption. However the lack of any correlations involving the

Balmer decrement (indicative of reddening by dust) suggests this may not be the solution. It is difficult to see how Seyfert galaxies that are bright in the 1/4 keV band, and so presumably contain little or no absorption, yet have weak permitted lines, are compatible with the standard Seyfert unification scheme (e.g., Antonucci 1993).

5 CONCLUSIONS

This paper presents the first complete sample of AGN selected on the basis of their $\sim 1/4$ keV flux. The sample comprises 54 Seyfert galaxies, 20 of which are identified as NLS1s on the basis that FWHM H$\beta \leq$2000 km s^{-1}.

The well-known anti-correlation between the strengths of Fe II and [O III] emission is detected, along with correlations between the soft X-ray slope and [O III] emission, Fe II strength and Hβ width. These suggest that the so-called 'primary eigenvector' found in other samples is a direct result of these optical lines being correlated with the soft X-ray spectral slope. Particularly interesting are the objects that lie at one end of the correlations, with relatively strong [O III] emission and weak optical continua, as these are rare in most other samples of soft X-ray selected AGN. Two of these objects are known to be X-ray transients, future observations are needed to confirm the nature of the other objects. The luminosity function for $\sim 1/4$ keV selected AGN is presented and these data are used to examine the relative densities of Seyferts as a function of Hβ line width and X-ray slope.

ACKNOWLEDGMENTS

The authors would like to thank Martin Ward and Paul O'Brien for useful discussions throughout the course of this work, the referee, Dirk Grupe, for a constructive referee's report, and the staff of the ING and Lick Observatories. This research made use of data obtained from the NASA/IPAC Extragalactic Database (NED), provided by NASA/JPL under contract with Caltech, from the Leicester Database and Archive Service (LEDAS) at the Department of Physics and Astronomy, Leicester University, UK, and from the Set of Identifications, Measurements and Bibliography for Astronomical Data (SIMBAD), maintained by the Centre de Donnees astronomiques de Strasbourg. SV acknowledges support from PPARC. The William Herschel Telescope is operated on the island of La Palma by the Isaac Newton Group in the Spanish Observatorio del Roque de los Muchachos of the Instituto de Astrofisica de Canarias, and the Lick Observatory 120″is operated by the University of California.

REFERENCES

Antonucci, R. R. J., 1993. ARA&A, **31**, 473.

Bade, N., Beckmann, V., Douglas, N. G., Barthel, P. D., Engels, D., Cordis, L., Nass, P. & Voges, W., 1998. A&A, **334**, 459.

Bade, N., Komossa, S. & Dahlem, M., 1996. A&A, **309**, L35.

Bedford, D. K., Vilhu, O. & Petrov, P., 1988. MNRAS, **234**, 319.

Boller, Th., Brandt, W. N. & Fink, H., 1996. A&A, **305**, 53.

Boller, Th., Trümper, J., Molendi, S., Fink, H., Schæidt, S., Caulet, A. & Dennefeld, M., 1993. A&A, **279**, 53.

Boroson, T. A. & Green, R. F., 1992. ApJ, **90**, 109.

Brandt, W. N. & Boller, T., 1998. *Astronomische Nachrichten*, **319**, 163.

Brandt, W. N., Pounds, K. A. & Fink, H., 1995. MNRAS, **273**, L47.

Dickey, J. M. & Lockman, F. J., 1990. ARA&A, **28**, 215.

Edelson, R., Vaughan, S., Warwick, R., Puchnarewicz, E. & George, I., 1999. MNRAS, **307**, 91.

Ferland, G. J. & Osterbrock, D. E., 1986. ApJ, **300**, 658.

Francis, P. J. & Wills, B. J., 1999. In: *ASP Conf. Ser. 162: Quasars and Cosmology*, Ferland, G. & Baldwin, J., eds., p. 363.

Francis, P. J., Hewett, P. C., Foltz, C. B. & Chaffee, F. H., 1992. ApJ, **398**, 476.

Gaskell, C. M., 1985. ApJ, **291**, 112.

Gaskell, C. M., 2000. *New Astronomy Review*, **44**, 563.

Goad, M., 2001. In: *Probing the Physics of Active Galactic Nuclei by Multiwavelength Monitoring*, Peterson, B. M., Polidan, R. S. & Pogge, R. W., eds., ASP Conferences Series, Vol 224, p. 431.

Grupe, D., Beuermann, K., Mannheim, K., Bade, N., Thomas, H. ., de Martino, D. & Schwope, A., 1995. A&A, **299**, L5.

Grupe, D., Beuermann, K., Thomas, H. C., Mannheim, K. & Fink, H. H., 1998a. A&A, **330**, 25.

Grupe, D., Wills, B. J., Wills, D. & Beuermann, K., 1998b. A&A, **333**, 827.

Grupe, D., Beuermann, K., Mannheim, K. & Thomas, H. C., 1999. A&A, **350**, 805.

Grupe, D., Thomas, H. . & Beuermann, K., 2001. A&A, **367**, 470.

Hasinger, G., Burg, R., Giacconi, R., Schmidt, M., Trumper, J. & Zamorani, G., 1998. A&A, **329**, 482.

Hasinger, G., Lehmann, I., Schmidt, M., Gunn, J. E., Schneider, D. P., Giacconi, R., Trümper, J. & Zamorani, G., 2000. *New Astronomy Review*, **44**, 497.

Haywood, M., Robin, A. C. & Creze, M., 1997. A&A, **320**, 440.

Horne, K., 1986. PASP, **98**, 609.

Komossa, S. & Bade, N., 1999. A&A, **343**, 775.

Krautter, J., Zickgraf, F. ., Appenzeller, I., Thiering, I., Voges, W., Chavarria, C., Kneer, R., Mujica, R., Pakull, M. W., Serrano, A. & Ziegler, B., 1999. A&A, **350**, 743.

Kuraszkiewicz, J., Wilkes, B. J., Brandt, W. N. & Vestergaard, M., 2000a. ApJ, **542**, 631.

Kuraszkiewicz, J., Wilkes, B. J., Czerny, B. . & Mathur, S., 2000b. ApJ, **542**, 692.

Laor, A., Fiore, F., Martin, E., Wilkes, B. J. & McDowell, J. C., 1997. ApJ, **477**, 93.

Lawrence, A., Elvis, M., Wilkes, B. J., McHardy, I. & Brandt, N., 1997. MNRAS, **285**, 879.

Lipari, S., Terlevich, R. & Macchetto, F., 1993. ApJ, **406**, 451.

Lockman, F. J., Jahoda, K. & McCammon, D., 1986. ApJ, **302**, 432.

Maccacaro, T., Gioia, I. M., Maccagni, D. & Stocke, J. T., 1984. ApJ, **284**, L23.

Marshall, H. L., 1985. ApJ, **299**, 109.

Oke, J. B. & Lauer, T. R., 1979. ApJ, **230**, 360.

Osterbrock, D. E. & Pogge, R. W., 1985. ApJ, **297**, 166.

Phillips, M. M., 1978. ApJ, **226**, 736.

Piccinotti, G., Mushotzky, R. F., Boldt, E. A., Holt, S. S., Marshall, F. E., Serlenitsos, P. J. & Shafer, R. A., 1982. ApJ, **253**, 485.

Pounds, K. A., Done, C. & Osborne, J. O., 1995. MNRAS, **277**, L5.

Pounds, K. A. *et al.*, 1993. MNRAS, **260**, 77.

Press, W. H., Teukolsky, S. A., Vetterling, W. T. & Flannery, B. P., 1992. *Numerical recipes in FORTRAN. The art of scientific computing*, Cambridge: University Press, c1992, 2nd ed.

Puchnarewicz, E. M. & Mason, K. O., 1998. MNRAS, **293**, 243.

Puchnarewicz, E. M. *et al.*, 1992. MNRAS, **256**, 589.

Puchnarewicz, E. M., Mason, K. O., Siemiginowska, A. & Pounds, K. A., 1995. MNRAS, **276**, 20.

Puchnarewicz, E. M., Mason, K. O. & Cordova, F. A., 1994. MNRAS, **270**, 663.

Schmidt, M. & Green, R. F., 1983. ApJ, **269**, 352.

Schmidt, M., Hasinger, G., Gunn, J., Schneider, D., Burg, R., Giacconi, R., Lehmann, I., MacKenty, J., Trumper, J. & Zamorani, G., 1998. A&A, **329**, 495.

Schmidt, M., 1968. ApJ, **151**, 393.

Schwope, A. D., Hasinger, G., Lehmann, I., Scharz, R., Brunner, H., Neizvestny, S., Ugryumov, A., Balega, Y., Trumper, J. & Voges, W., 2000. *Astronomische Nachrichten*, **321**, 1.

Stephens, S. A., 1989. AJ, **97**, 10.

Strassmeier, K. G., Hall, D. S., Fekel, F. C. & Scheck, M., 1993. A&AS, **100**, 173.

Thomas, H. ., Beuermann, K., Reinsch, K., Schwope, A. D., Truemper, J. & Voges, W., 1998. A&A, **335**, 467.

Trümper, J. *et al.*, 1991. *Nature*, **349**, 579.

Vallenari, A., Bertelli, G. & Schmidtobreick, L., 2000. A&A, **361**, 73.

Vaughan, S., 2001. *PhD thesis*, University of Leicester.

Vennes, S., Thejll, P. A., Galvan, R. G. & Dupuis, J., 1997. ApJ, **480**, 714.

Véron-Cetty, M. P., Véron, P. & Gonçalves, A. C., 2001. A&A, **in press**, astro ph/0104151.

Voges, W. *et al.*, 1999. A&A, **349**, 389.

Wills, B., 1982. In: *IAU Symp. 97: Extragalactic Radio Sources*, p. 373.

Zheng, W. & O'Brien, P. T., 1990. ApJ, **353**, 433.

APPENDIX A: SOFT X-RAY BRIGHT SUBSAMPLES

Table A1 lists the subsamples of BL Lacertae objects and Clusters and Table A2 lists the subsample of Galactic objects selected as described in Section 2.

APPENDIX B: NEW OPTICAL OBSERVATIONS OF THE SEYFERT SAMPLE

The new optical spectra were obtained with the 4.2m William Herschel Telescope (WHT) at the Observatario Roque de los Muchachos on the Island of La Palma, on the nights of 1999 March 21 and 22, and with the 3.0m Shane Telescope at Lick Observatory, Mt. Hamilton, California from 1999 May 21–23.

The WHT observations used the ISIS spectrograph[§] with the R300B grating and a EEV 42 CCD camera on the blue arm and the R158R grating with a TEK 2 CCD camera on the red arm. The combination of blue and red spectra provided coverage from 3600Å to 9000Å. The Shane data were obtained with the Kast spectrograph[¶] using grism #2 and grating #6 in the blue and red arms respectively, both with Reticon 1200x400 CCD cameras. This set-up provided similar wavelength coverage (3500Å–9000Å) to the WHT data.

The data were extracted following standard procedures using IRAF[‖]. Individual frames were bias subtracted and flat-field corrected. Spectra were traced on the CCD using a low-order polynomial and then optimally extracted (Horne 1986) using a variable extraction slit-width (typically $4''$). Background regions for sky subtraction were located where possible either side of the target spectrum. Sky-line and cosmic ray removal occurs during the extraction procedure. Extracted spectra were wavelength calibrated, corrected

[§] See `http://www.ing.iac.es/~bgarcia/isis_new/isis_home.html`

[¶] See `http://www.ucolick.org/~mountain/mthamilton/techdocs/instruments/kast/kast_index.html`

[‖] IRAF is the Image Reduction and Analysis Facility and is written and supported by the IRAF programming group at the National Optical Astronomy Observatories (NOAO) in Tucson, Arizona. See `http://iraf.noao.edu/iraf/web/`

Table A1. The BL Lac and cluster samples. The columns provide the following information: (2) The source name; (3) the source type; (4) the redshift; (5) and (6) the right ascension and declination as tabulated in the RBSC; (7) the full-band count rate; (8) the hardness ratio $HR1$; (9) the Galactic column; (10) and (11) the derived C- and H-band count rates.

No	Name	Type	z	R.A. (J2000)	Dec. (J2000)	T (ct/s)	$HR1$	N_H (10^{20} cm^{-2})	C (ct/s)	H (ct/s)
(1)	(2)	(3)	(4)	(5)	(6)	(7)	(8)	(9)	(10)	(11)
1	1ES 0927+5	BL Lac	0.190	09 30 37	49 50 28	2.15±0.07	0.06±0.03	1.40	1.012	1.142
2	RX J1008+47	BL Lac	0.343	10 08 11	47 05 26	1.10±0.05	-0.29±0.04	0.88	0.711	0.392
3	B3 1009+427	BL Lac	0.364	10 12 44	42 29 58	0.66±0.04	0.02±0.05	1.09	0.325	0.339
4	GB 1011+496	BL Lac	0.2	10 15 04	49 26 04	1.94±0.07	-0.38±0.03	0.79	1.340	0.602
5	RX J1016+41	BL Lac	0.281	10 16 16	41 08 17	0.48±0.03	-0.08±0.06	1.14	0.259	0.221
6	1ES 1028+511	BL Lac	0.361	10 31 18	50 53 40	4.46±0.09	-0.26±0.02	1.17	2.812	1.652
7	87GB 10553	BL Lac	0.144	10 58 37	56 28 16	0.46±0.03	-0.48±0.05	0.67	0.340	0.119
8	FIRST J110	BL Lac	–	11 00 21	40 19 33	0.61±0.04	-0.35±0.06	1.16	0.410	0.198
9	Mrk 421	BL Lac	0.03	11 04 27	38 12 31	26.57±0.28	-0.21±0.01	0.71	16.075	10.495
10	87GB 11051	BL Lac	–	11 07 48	15 02 17	0.45±0.04	-0.19±0.08	1.49	0.270	0.184
11	87GB 11429	BL Lac	0.138	11 17 06	20 14 10	4.34±0.12	-0.01±0.02	1.36	2.191	2.147
12	Mrk 180	BL Lac	0.046	11 36 26	70 09 32	4.53±0.08	-0.20±0.01	1.42	2.719	1.813
13	87GB 11333	BL Lac	0.135	11 36 30	67 37 08	1.91±0.06	0.07±0.03	1.35	0.886	1.020
14	Ton 116	BL Lac	–	12 43 12	36 27 42	1.30±0.05	-0.36±0.03	1.36	0.882	0.415
15	PG 1246+586	BL Lac	–	12 48 18	58 20 31	0.52±0.04	-0.42±0.06	1.12	0.366	0.150
16	1ES 1255+244	BL Lac	0.141	12 57 31	24 12 45	0.93±0.05	-0.10±0.05	1.26	0.513	0.420
17	RX J1302+50	BL Lac	0.688	13 02 55	50 56 21	0.52±0.04	-0.05±0.06	1.18	0.274	0.248
18	RX J1341+39	BL Lac	0.163	13 41 04	39 59 42	0.76±0.04	-0.10±0.04	0.80	0.416	0.340
19	RX J1420+53	BL Lac	–	14 20 24	53 34 03	0.29±0.02	-0.92±0.03	1.18	0.275	0.011
20	RX J1442+58	BL Lac	0.638	14 22 39	58 01 59	2.0±0.06	-0.09±0.02	1.32	1.090	0.910
21	H 1426+428	BL Lac	0.129	14 28 32	42 40 28	4.20±0.09	-0.06±0.02	1.38	2.228	1.975
22	PG 1437+398	BL Lac	–	14 39 17	39 32 48	1.43±0.05	-0.35±0.03	1.05	0.966	0.465
23	[WB92] 144	BL Lac	–	14 48 01	36 08 33	0.60±0.04	-0.54±0.05	1.05	0.460	0.137
24	1ES 1533+535	BL Lac	0.89	15 35 01	53 20 42	1.43±0.04	0.00±0.02	1.32	0.716	0.716
25	RX J1631+42	BL Lac	0.468	16 31 24	42 16 56	0.53±0.03	-0.07±0.04	1.04	0.282	0.245
1	ABELL 1656	Cluster	0.023	12 59 47	27 56 35	11.70±0.13	0.33±0.05	0.92	3.920	7.781
2	ABELL 1795	Cluster	0.062	13 48 52	26 35 40	3.77±0.09	0.28±0.02	1.19	1.358	2.415
3	ABELL 1914	Cluster	0.171	14 26 01	37 49 35	0.91±0.04	0.25±0.04	0.95	0.342	0.571
4	ABELL 2129	Cluster	0.030	16 28 37	39 32 48	4.5±0.08	0.30±0.01	0.86	1.575	2.925

for atmospheric extinction and flux calibrated by comparison with a photometric standard.

Multiple exposures of the same object were combined where possible prior to extraction in order to increase the signal-to-noise ratio and help remove cosmic ray contamination. However, this was not possible in cases where only one exposure was taken or when target source image moved across the CCD chip between exposures, in which case the data were extracted separately from each frame and then combined.

The absolute fluxes of the separate blue and red spectra for each object generally match to within 10 per cent. One source, RX J1619+40, was observed at both observatories to allow a test of the flux calibration. The two sets of spectra match to within 20 per cent over the useful wavelength range. Given that the source may have varied between the two observations (separated by 2 months) it seems reasonable to conclude that the absolute flux calibration of these data are good to within 20 per cent, a value which is typical of optical spectroscopy obtained under non-photometric conditions. The spectral resolution of the data were estimated from fits to the intrinsically narrow arc lamp lines. For the WHT data the blue spectra have a FWHM $\sim$ 3.5 Å and the red have FWHM $\sim$ 5 Å, the Shane data have FWHM of 4 Å and 8 Å in the blue and red respectively. These correspond to a velocity width $\sim$ 200 km/s at [O III] λ5007.

Before any measurements were taken from the optical data, the red and blue spectra for each object were combined into one spectrum. The data were convolved with a Gaussian (of width smaller than the spectral resolution) in order to smooth out any remaining bad pixels (but without degrading the spectral resolution). The blue data were then scaled to match the flux of the red data in the region of overlap, which was typically 350 Å wide for the Shane data but only $\lesssim$ 100 Å for the WHT data. (The red data were chosen as the flux norm simply because the signal-to-noise is higher in the red arm than it is in the blue.) The data were then combined and averaged in the overlap region to produce a single, continuous blue-red spectrum.

Due to the small overlap between blue and red spectra in the WHT observations, the normalisation between blue and red is rather less accurate than in the case of the Shane data, and forcing continuity between blue and red may introduce a systematic error in the shape of the spectrum in the overlapping region. For most sources this has no effect on the derived spectral properties, but if, as in the case of RX J1054+48, the Hβ line falls in the overlap region then the detailed profile of the line will be distorted somewhat. This is unavoidable as the line falls at the far end of each spectrum,

Table A2. The Galactic sample. The columns provide the following information: (2) the source name; (3) and (4) the right ascension and declination as tabulated in the RBSC; (5) the full-band count rate; (6) hardness ratio; (7) Galactic column; (8) and (9) derived C- and H-band count rates; (10 and (11) the source type and optical magnitude (V-band where available).

No. (1)	Name (2)	R.A. (J2000) (3)	Dec (J2000) (4)	T (ct/s) (5)	$HR1$ (6)	N_H (10^{20} cm^{-2}) (7)	C (ct/s) (8)	H (ct/s) (9)	Type (10)	Mag (11)
1	HD76943 B	09 00 38	41 47 02	0.68±0.05	-0.46±0.05	1.29	0.493	0.183	F5V	4.0
2	HR 3922	09 57 12	57 25 12	0.62±0.03	0.09±0.05	1.08	0.280	0.336	G5III	6.0
3	G 196-3	10 04 21	50 23 17	0.69±0.04	-0.26±0.05	0.82	0.434	0.255	M3Ve	13.3
4	RE J1032+53	10 32 10	53 29 40	5.07±0.10	-1.00±0.00	1.16	5.069	0.000	WD/DA	14.5
5	RE J1043+49	10 43 11	49 02 27	0.93±0.05	-1.00±0.00	1.32	0.930	0.000	WD	16.1
6	FH Uma	10 47 10	63 35 22	0.26±0.02	-0.97±0.01	1.06	0.253	0.004	CV/AM Her	19.4
7	EK Uma	10 51 35	54 04 37	1.11±0.05	-0.99±0.00	0.98	1.103	0.006	CV/AM Her	18.0
8	DM Uma	10 55 43	60 28 10	0.90±0.04	-0.19±0.04	0.68	0.534	0.363	K0/RSCVN	9.3
9	LB 1919	10 59 16	51 24 52	4.18±0.09	-0.99±0.00	1.06	4.159	0.021	WD/DA	16.8
10	HD 95559	11 02 02	22 35 46	1.01±0.07	0.01±0.07	1.41	0.498	0.509	G5III	8.9
11	AN Uma	11 04 25	45 03 19	1.77±0.07	-0.94±0.01	1.11	1.718	0.053	CV/AM Her	15.5
12	Ton 61	11 12 38	24 09 09	0.61±0.05	-0.96±0.03	1.23	0.596	0.012	WD/DA	15.1
13	PG 1234+48	12 36 45	47 55 30	1.45±0.06	-1.00±0.00	1.19	1.451	0.000	WD/sd:B	14.4
14	31 Com	12 51 42	27 32 21	1.11±0.09	0.31±0.07	0.90	0.382	0.724	G0IIIp	4.9
15	Gl 490	12 57 40	35 13 34	0.84±0.04	-0.22±0.04	1.23	0.511	0.327	M0.5e	10.3
16	RS CVn	13 10 36	35 56 04	0.89±0.04	0.04±0.04	1.03	0.425	0.461	F4v+RSCVn	8.2
17	HZ 43	13 16 21	29 05 55	72.84±0.32	-0.99±0.00	1.08	72.470	0.364	WD/DA	12.7
18	HD 116204	13 21 32	38 52 49	1.32±0.05	0.22±0.03	0.97	0.513	0.803	G8III/RSCVn	7.3
19	GJ 3789	13 31 46	29 16 31	0.41±0.03	-0.32±0.07	1.16	0.271	0.139	M4	12.0
20	BD +23 258	13 32 41	22 30 07	0.84±0.05	-0.13±0.05	1.44	0.477	0.367	KV	9.6
21	HR 5110	13 34 47	37 10 59	2.77±0.08	-0.07±0.02	0.92	1.481	1.287	F2IV/RSCVn	4.9
22	RX J1342+28	13 42 10	28 22 50	0.58±0.04	-0.95±0.02	1.14	0.561	0.014	SSS/Glob Cl	–
23	HD 123351	14 06 26	30 50 51	0.81±0.05	0.00±0.05	1.25	0.405	0.405	K0	7.6
24	HR 5404	14 25 11	51 51 09	2.00±0.06	0.02±0.02	1.29	0.978	1.018	F7V	4.1
25	RX J1605+54	16 05 18	54 21 01	0.50±0.02	-0.11±0.04	1.23	0.278	0.223	M	19.1
26	HD 146696	16 15 43	44 33 10	0.58±0.04	0.07±0.06	1.15	0.271	0.312	G0	8.9
27	GJ 9557A	16 19 55	39 42 23	0.64±0.03	-0.16±0.04	0.93	0.371	0.269	F0V	5.5

where the calibration is worst, and the small overlap means that neither spectrum contains the complete line profile.

B1 Optical measurements

The optical spectra were used to measure the basic optical properties of each object. Redshifts were obtained from the identification papers or derived from fitting a Gaussian to the upper half of the observed [O III] λ5007 line in each spectrum. (The centroid of a Gaussian fit and the line peak were generally consistent within the limits set by the spectral resolution of the data.)

B1.1 Fe II *subtraction*

In many of these spectra there is a clear contribution from blends of Fe II line emission on both the blue and red sides of the Hβ-[O III] complex. An automatic fitting routine developed by Goad (2001) (based on the method of BG92) was used to estimate the strength of these lines, and remove any Fe II contamination from the Hβ region.

The method involves comparing a template optical Fe II line spectrum with the observed spectra. The template used in the present work was the same as that of BG92, namely the Fe II lines of the bright NLS1 I Zw 1, which shows very strong and narrow permitted Fe II emission (e.g., Phillips 1978; Oke & Lauer 1979). The template was redshifted to match the source, smoothed (by convolving with a Gaussian), and scaled to fit the data either side of Hβ. (The convolution was carried out over a wavelength range broad enough that edge effects are not significant). The four free parameters in the fit were: the strength of the Fe II emission, the width of the convolution kernel (broadening parameter), and two parameters describing a 1st order polynomial used to model the continuum local to Hβ. (Where possible the region around He II λ4686 was ignored in the fit, although in some cases the He II emission may be broad and this will effect the fit.) The best-fit optical Fe II spectrum was then subtracted from the data. The Fe II flux was measured between λ4434 and λ4684 as in BG92. (Note that when Fe II measurements were taken from the literature, they were scaled by a factor, derived from the I Zw 1 template, to take into account the different in wavelength ranges used to define Fe II flux.)

The Hβ–[O III] regions of all the observed objects, before and after Fe II subtraction, are shown in Figure B1. The procedure described above generally did a reasonable job of estimating the strength of the Fe II emission and decontaminating the optical spectrum. There are three obvious exceptions however. In both RX J1050+55 and RX J1054+48 the part of the spectrum containing the Hβ line is redshifted into the region between the blue and red WHT spectra, and as the overlap between the two spectra is not well determined it is difficult to accurately measure the surround-

ing Fe II emission. In the highest redshift member of the sample, RX J1046+52, the Hβ–[O III] region is affected by strong A-band telluric absorption.

As mentioned above, the width of the Fe II lines in the fit was left as a free parameters. I Zw 1 has FWHM H$\beta\sim$ 900 km s^{-1}, and has Fe II lines of comparable width. This means that it was not possible to accurately model optical Fe II emission narrower than 900 km s^{-1}. As there are very few Seyfert 1s with FWHM H$\beta\lesssim$ 900 km s^{-1} this posed no serious problem. (The results of this fitting agree with the claim of BG92 that the Hβ and optical Fe II lines have similar widths.) The other limitation of this method is that it assumes the ratios of the optical Fe II lines within and between blends are the same as those in I Zw 1. This appears to be a reasonable approximation for most objects, but a few (e.g., PG 1415+451) may show slightly different ratios.

B1.2 Other line measurements

The other optical properties were measured from the dereddened, Fe II subtracted spectra using the `DIPSO` software package. To measure line fluxes local straight-line continua were fitted and subtracted from underneath the lines and the remaining line flux was integrated. In many cases there is a clear contribution to Hβ from a separate narrow component. In order to measure the properties of only the broad Hβ line, a narrow Hβ component was constructed, with a width determined from fitting the narrow [O III] lines, and included in a multiple Gaussian fit to the Hβ line. In most spectra the narrow component could be isolated and removed before the properties of the broad Hβ line were measured. The Hα line contains contributions from [N II] λ6548, 6584 which in general could not be isolated in these data. Here, as in Grupe *et al.* (1999), the [N II] flux is subtracted by assuming that these lines contribute 35% of the flux in [O III] λ5007, following Ferland & Osterbrock (1986).

B1.3 Continuum measurements

The continuum level at the positions of Hβ λ4861 and Hα λ6563 were measured from the Fe II subtracted spectra, and further continuum fluxes were measured at 4000, 5500 and 7000 Å(in the rest frame of the source). The equivalent widths of the Hβ, [O III] and Fe II lines were calculated with respect to the continuum underneath Hβ to allow direct comparison with the measurements of BG92 and Grupe *et al.* (1999). Two spectral indices ($S_\nu \propto \nu^{-\alpha}$) were constructed from these flux measurements, namely:

$$\alpha_{opt} = 4.11\ \log(\frac{f_{7000\mathring{\rm A}}}{f_{4000\mathring{\rm A}}})$$

$$\alpha_{OX} = 0.489\ \log(\frac{f_{5500\mathring{\rm A}}}{f_{0.25{\rm keV}}})$$

These indices are almost identical to those used in Grupe *et al.* (1998a). In seven cases where the λ5500 flux is not available it was derived in an approximate way from m_V (column 13 of Table 1). Assuming that the uncertainty in flux ratios is $\sim$ 10% leads to an uncertainty of ~ 0.27 in α_{opt} and ~ 0.03 in α_{OX} and

Table B1 lists the derived parameters. The columns list the following information: (3) FWHM of broad Hβ; (4) FWHM of [O III] λ5007; (5), (6) and (7) list the local equivalent widths of the Hβ, Fe II and [O III] λ5007 lines; (8) Balmer decrement, i.e., the ratio of fluxes in Hα/Hβ; (9) ratio of the peak fluxes of [O III] λ5007 and broad Hβ; (10) and (11) ratio of fluxes of [O III] and Fe II to broad Hβ; (12) and (13) spectral indices defined above; (14) the monochromatic 0.25 keV luminosity in νL_ν units (in the rest frame of the source).

Table B1. Properties of the sources which comprise the 1/4 keV-selected Seyfert galaxy sample.

No (1)	Name (2)	Hβ FWHM (km/s) (3)	[O III] FWHM (km/s) (4)	Hβ EW (Å) (5)	Fe II EW (Å) (6)	[O III] EW (Å) (7)	Hα/ Hβ (8)	peak [O III]/ Hβ (9)	[O III]/ Hβ (10)	Fe II/ Hβ (11)	α_{opt} (12)	α_{OX} (13)	$\log(\nu L_{1/4})$ erg/s (14)
1	1E 0919+515	1390	-	38	78	-	-	-	-	2.05	-	0.9	44.5
2	Mrk 110	2120	-	145	20	3	-	2.5	0.7	0.14	-	0.9	43.9
3	US 0656	-	-	-	-	-	-	-	-	-	-	1.0	44.8
4	PG 0953+414	3130	-	156	39	19	-	0.8	0.1	0.25	-	1.4	45.2
5	IRAS 10026+4347	2990	825	55	99	5	-	-	0.1	1.81	0.1	1.1	44.8
6	RX J1008+46	13645	765	120	0	31	-	4.4	0.3	0.00	-	0.8	45.4
7	Ton 1187	2850	370	76	33	22	3.5	-	0.3	0.43	-	1.2	44.5
8	RX J1019+37	1130	675	75	0	26	2.8	5.9	0.3	0.00	1.3	0.8	44.8
9	Mrk 141	4175	395	30	38	16	3.8	-	0.5	1.25	1.5	1.3	43.4
10	Mrk 142	1790	280	52	86	10	3.3	-	0.2	1.65	1.2	0.9	44.0
11	RX J1026+55	5035	530	183	78	29	1.7	2.2	0.2	0.43	1.6	1.1	44.1
12	RE J1034+396	1500	900	60	-	45	3.0	-	0.8	-	-	1.0	44.0
13	RX J1046+52	2670	-	29	-	-	-	-	-	-	-	1.1	45.4
14	RX J1050+55	2780	760	51	0	23	5.0	1.6	0.5	0.00	1.5	1.2	45.1
15	RX J1054+48	5210	1115	71	0	18	3.6	1.2	0.3	0.00	-0.2	1.3	45.2
16	EXO 1055+60	2155	540	90	110	25	-	-	0.3	1.27	1.3	1.2	44.2
17	RX J1117+65	2160	880	65	78	11	-	-	0.2	1.20	1.2	1.1	44.5
18	PG 1116+21	2920	-	175	81	11	-	0.3	0.1	0.46	-	1.2	45.1
19	EXO 1128+691	1800	-	10	-	-	-	-	-	-	-	0.8	44.0
20	RX J1138+57	2845	485	39	56	25	3.3	3.7	0.6	1.43	0.5	0.9	44.4
21	NGC 4051	990	-	-	-	-	-	-	-	-	-	1.8	41.8
22	RX J1209+32	1370	860	63	67	28	3.5	0.9	0.4	1.06	0.6	0.9	44.5
23	RX J1226+32	3940	640	66	0	43	5.0	3.9	0.6	0.00	1.4	0.9	45.0
24	RX J1232+49	1905	895	55	92	9	4.5	0.3	0.2	1.67	0.9	0.9	44.9
25	Ton 83	1435	670	92	38	13	3.5	0.4	0.1	0.41	0.6	1.0	45.4
26	MCG +8-23-067	1245	645	30	0	41	3.6	2.6	1.4	0.00	2.5	1.0	43.2
27	IC 3599	675	615	9	0	18	3.7	2.3	2.1	0.00	1.8	0.7	43.7
28	Was 61	2765	740	30	62	55	6.8	6.7	1.8	2.09	2.6	1.1	43.8
29	RX J1244+58	720	785	56	47	11	3.3	0.3	0.2	0.84	0.3	0.9	44.5
30	RX J1258+23	6920	420	29	25	34	4.0	18.6	1.2	0.86	2.8	1.0	43.9
31	RX J1312+26	3530	535	20	12	3	2.7	1.1	0.2	0.58	1.5	1.1	43.6
32	Ton 1571	1330	650	59	86	10	2.7	0.4	0.2	1.47	0.7	1.2	43.8
33	RX J1319+52	1620	415	29	45	35	4.0	4.5	1.2	1.53	1.1	0.9	44.2
34	RX J1328+24	2370	610	65	25	20	4.4	1.2	0.3	0.39	0.8	1.1	44.7
35	IRAS 13349+243	2775	1340	54	76	7	4.8	0.3	0.1	1.41	1.1	1.3	44.9
36	RX J1339+40	1180	425	21	9	9	3.5	1.1	0.4	0.43	1.4	0.9	44.1
37	RX J1342+38	4290	385	75	12	45	3.7	6.5	0.6	0.16	0.8	0.8	44.6
38	PG 1341+25	3300	440	60	43	18	3.9	2.1	0.3	0.72	1.0	1.2	44.0
39	Mrk 663	-	770	0	0	11	-	-	-	-	3.5	1.1	43.4
40	RX J1355+56	2600	935	44	46	46	4.8	5.0	1.8	1.05	0.5	1.1	44.4
41	PG 1402+261	2220	-	74	168	$<$1.8	-	$<$0.6	$<$0.02	2.25	-0.5	1.1	44.8
42	PG 1415+451	2575	-	69	132	$<$5.6	2.6	$<$0.03	$<$0.07	1.91	0.5	1.3	44.2
43	RX J1426+39	-	-	-	-	-	-	-	-	-	-	1.3	43.8
44	Mrk 684	1170	-	45	82	$<$1.1	2.0	$<$0.09	$<$0.02	1.81	0.9	1.3	43.7
45	Mrk 478	1915	610	65	87	12	3.7	-	0.2	1.34	0.7	0.9	44.9
46	PG 1444+407	2775	-	141	135	$<$7.3	2.5	$<$0.14	$<$0.04	0.96	-0.1	1.2	45.0
47	RX J1448+35	2430	625	54	64	24	3.1	1.7	0.4	1.18	0.5	1.3	44.0
48	NGC 5905	405	415	3	0	2	10.9	0.4	0.5	0.00	2.7	1.7	41.7
49	RX J1529+56	4055	540	100	8	170	3.8	12.5	1.7	0.08	0.9	1.1	44.4
50	MCG +06-36-003	6320	420	100	35	34	3.3	5.0	0.3	0.35	1.2	1.2	43.9
51	RX J1618+36	1705	390	20	23	13	2.9	2.7	0.6	1.14	1.7	1.0	43.5
52	RX J1619+40	3330	650	44	35	29	2.9	3.2	0.7	0.81	1.5	1.1	43.2
53	RX J1629+40	2675	750	55	36	32	3.0	1.6	0.6	0.64	0.4	0.9	45.1
54	RX J1646+39	1515	800	84	40	22	2.0	0.7	0.3	0.47	1.0	1.1	44.2

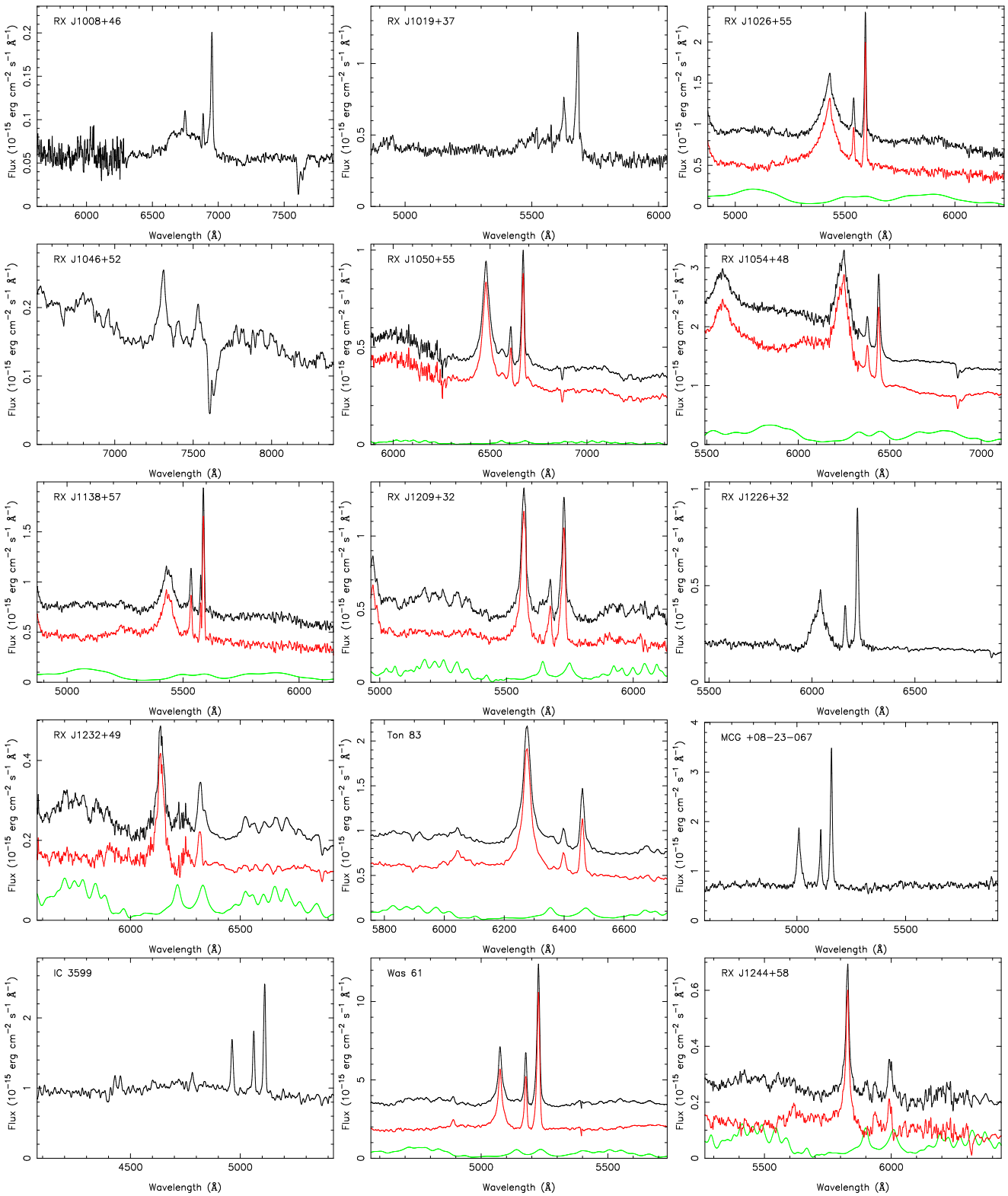

Figure B1. Close-up of the Hβ–[O III] region showing the fitted Fe II emission. In each panel the topmost curve shows the original spectrum, the middle curve shows the spectrum after Fe II subtraction and the lower curve shows the blurred Fe II template. Objects with no measurable Fe II emission are shown with only one curve. The topmost curve is shifted upwards by an arbitrary amount for clarity.

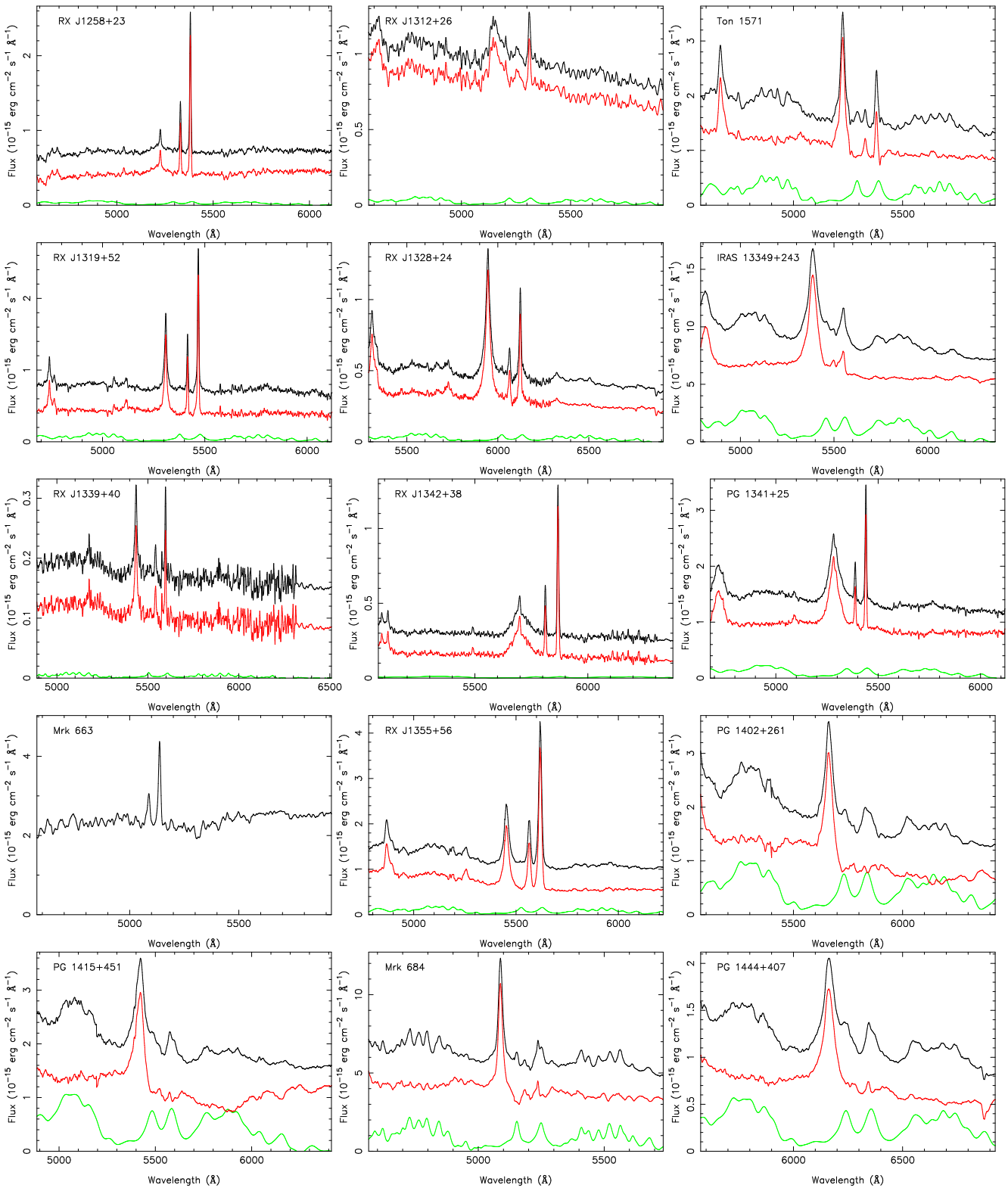
RX J1258+23
RX J1312+26
Ton 1571
RX J1319+52
RX J1328+24
IRAS 13349+243
RX J1339+40
RX J1342+38
PG 1341+25
Mrk 663
RX J1355+56
PG 1402+261
PG 1415+451
Mrk 684
PG 1444+407
Flux (10^{-15} erg cm^{-2} s^{-1} Å^{-1})
Wavelength (Å)

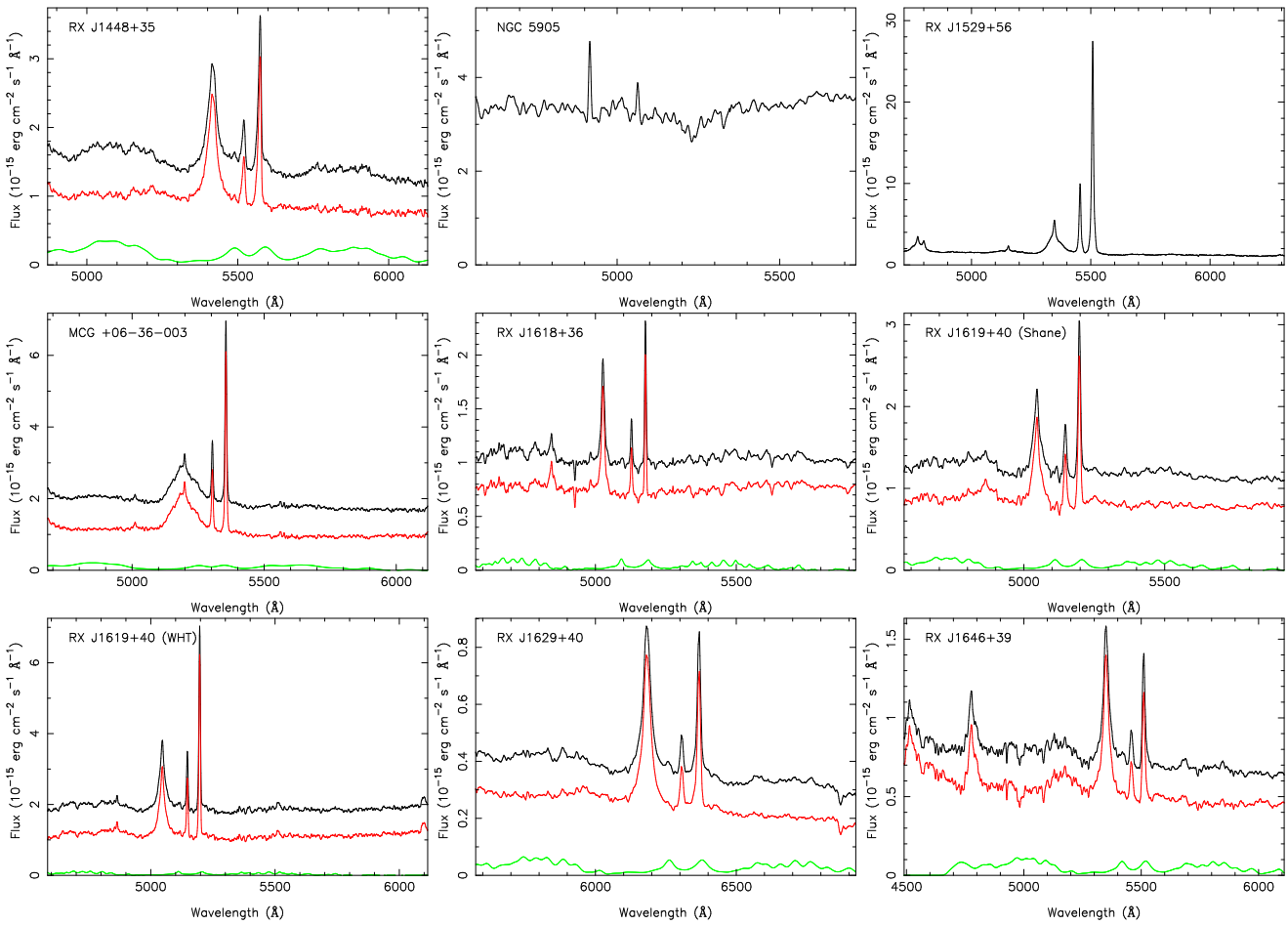
RX J1448+35
NGC 5905
RX J1529+56
MCG +06−36−003
RX J1618+36
RX J1619+40 (Shane)
RX J1619+40 (WHT)
RX J1629+40
RX J1646+39
Flux (10^{-15} erg cm^{-2} s^{-1} Å^{-1})
Wavelength (Å)